The Astrophysical Journal, 889:169 (13pp), 2020 February 1 https://doi.org/10.3847/1538-4357/ab6336

Gamma-Ray Emission of ^{60}Fe and ^{26}Al Radioactivity in Our Galaxy

W. Wang[1,2], T. Siegert[3,4], Z. G. Dai[1,5], R. Diehl[4,6], J. Greiner[4], A. Heger[7,8], M. Krause[9], M. Lang[4], M. M. M. Pleintinger[4], and X. L. Zhang[4]

[1] School of Physics and Technology, Wuhan University, Wuhan 430072, People's Republic of China; wangwei2017@whu.edu.cn, dzg@nju.edu.cn
[2] WHU-NAOC Joint Center for Astronomy, Wuhan University, Wuhan 430072, People's Republic of China
[3] Center for Astrophysics and Space Sciences, UC San Diego, La Jolla, CA 92093-0424, USA; tsiegert@ucsd.edu
[4] Max-Planck-Institut für extraterrestrische Physik, D-85741 Garching, Germany; rod@mpe.mpg.de
[5] School of Astronomy and Space Science, Nanjing University, Nanjing 210093, People's Republic of China
[6] Munich Cluster of Excellence "Universe," D-85748 Garching, Germany
[7] School of Physics and Astronomy, Monash University, VIC 3800, Australia
[8] Tsung-Dao Lee Institute, Shanghai 200240, People's Republic of China
[9] Centre for Astrophysics, University of Hertfordshire, Hatfield, AL10 9AB, UK

Received 2019 September 29; revised 2019 December 15; accepted 2019 December 15; published 2020 February 4

Abstract

The isotopes ^{60}Fe and ^{26}Al originate from massive stars and their supernovae, reflecting ongoing nucleosynthesis in the Galaxy. We studied the gamma-ray emission from these isotopes at characteristic energies 1173, 1332, and 1809 keV with over 15 yr of SPI data, finding a line flux in ^{60}Fe combined lines of $(0.31 \pm 0.06) \times 10^{-3}$ ph cm^{-2} s^{-1} and the Al line flux of $(16.8 \pm 0.7) \times 10^{-4}$ ph cm^{-2} s^{-1} above the background and continuum emission for the whole sky. Based on the exponential disk grid maps, we characterize the emission extent of ^{26}Al to find scale parameters $R_0 = 7.0^{+1.5}_{-1.0}$ and $z_0 = 0.8^{+0.3}_{-0.2}$ kpc; however, the ^{60}Fe lines are too weak to spatially constrain the emission. Based on a point-source model test across the Galactic plane, the ^{60}Fe emission would not be consistent with a single strong point source in the Galactic center or somewhere else, providing a hint of a diffuse nature. We carried out comparisons of emission morphology maps using different candidate source tracers for both ^{26}Al and ^{60}Fe emissions and suggest that the ^{60}Fe emission is more likely to be concentrated toward the Galactic plane. We determine the ^{60}Fe/^{26}Al γ-ray flux ratio at $18.4\% \pm 4.2\%$ when using a parameterized spatial morphology model. Across the range of plausible morphologies, it appears possible that ^{26}Al and ^{60}Fe are distributed differently in the Galaxy. Using the best-fitting maps for each of the elements, we constrain flux ratios in the range 0.2–0.4. We discuss the implications for massive star models and their nucleosynthesis.

Unified Astronomy Thesaurus concepts: Gamma-rays (637); Gamma-ray astronomy (628); Gamma-ray sources (633)

1. Introduction

The radioactive isotope ^{60}Fe is produced in suitable astrophysical environments through successive neutron captures on preexisting Fe isotopes such as (stable) ^{54,56,57,58}Fe in a neutron-rich environment. Candidate regions for ^{60}Fe production are the He- and C-burning shells inside massive stars, where neutrons are likely to be released from the ^{22}Ne(α,n) reaction. Production of ^{60}Fe may occur any time during the late evolution of massive stars toward core-collapse supernovae (Woosley & Weaver 1995; Limongi & Chieffi 2003, 2006, 2013; Pignatari et al. 2016; Sukhbold et al. 2016; and references therein). There is also an explosive contribution to the ^{60}Fe yield by the supernova shock running through the carbon and helium shells (Rauscher et al. 2003). Electron-capture supernovae may be the most significant producer of ^{60}Fe in the Galaxy (Wanajo et al. 2013, 2018; Jones et al. 2016, 2019a). There are other possible astrophysical sources of ^{60}Fe. From similar considerations, ^{60}Fe can also be made and released in super-asymptotic giant branch (AGB) stars (Lugaro et al. 2012). Furthermore, high-density Type Ia supernova explosions that include a deflagration phase (Woosley 1997) can produce even larger amounts per event.

Due to its long lifetime (radioactive half-life $T_{1/2} \simeq 2.6$ Myr; Rugel et al. 2009; Wallner et al. 2015; Ostdiek et al. 2017), ^{60}Fe survives to be detected in γ-rays after being ejected into the interstellar medium: ^{60}Fe β-decays to ^{60}Co, which decays within 5.3 yr to ^{60}Ni, into an excited state that cascades into its ground state by γ-ray emission at 1173 and 1332 keV. There is a similarly long radioactive lifetime of $\sim 10^6$ yr for ^{26}Al, and it was the first live radioactive isotope detected in characteristic γ-rays at 1809 keV (Mahoney et al. 1982), thus proving currently ongoing nucleosynthesis in our Galaxy. Mapping the diffuse ^{26}Al γ-ray emission suggested that it follows the overall Galactic massive star population (Diehl et al. 1995; Prantzos & Diehl 1996). If ^{60}Fe and ^{26}Al have similar astrophysical origins, with their similar radioactive lifetimes, the ratio of ^{60}Fe to ^{26}Al γ-ray emissions in the Galaxy would be independent of the true specific distances and locations of the sources and thus important for testing stellar evolution models with their nucleosynthesis and core-collapse supernova endings (Woosley & Heger 2007; Diehl 2013).

The steady-state mass of these radioactive isotopes maintained in the Galaxy through such production counterbalanced by radioactive decay thus converts into a ratio for the γ-ray flux in each of the two lines through

$$\frac{I(^{60}\mathrm{Fe})}{I(^{26}\mathrm{Al})} \sim 0.43 \cdot \frac{\dot{M}(^{60}\mathrm{Fe})}{\dot{M}(^{26}\mathrm{Al}}. \quad (1)$$

Timmes et al. (1995) carried the massive star yields into an estimate of chemical evolution for ^{60}Fe and ^{26}Al in the Galaxy, predicting a γ-ray flux ratio of 0.16. Various revisions of models presented different ratio values ($\sim$0.5–1; see Rauscher et al. 2002; Limongi & Chieffi 2003, 2006; Prantzos 2004; Woosley & Heger 2007). Different massive star regions, such as Scorpius–Centaurus or Cygnus, may show a different ^{60}Fe/^{26}Al ratio, as the

age of such associations dictates the expected fluxes (Voss et al. 2009). The average over the whole Milky Way, on the other hand, is determined by the number of massive stars and their explosions over the characteristic lifetimes of ^{26}Al and ^{60}Fe, respectively, providing an independent measure of the core-collapse supernova rate in the Milky Way and up to what masses stars actually explode.

The yields of these two isotopes depend sensitively on not only the stellar evolution details, such as shell burning and convection, but also the nuclear reaction rates. Tur et al. (2010) found that the production of ^{60}Fe and ^{26}Al is sensitive to the 3α reaction rates during He burning; i.e., the variation of the reaction rate by a factor of 2 will make a factor of nearly 10 change in the ^{60}Fe/^{26}Al ratio. The ^{60}Fe may be destroyed within its source by further neutron captures, ^{60}Fe(n, γ). Since its closest parent, ^{59}Fe, is unstable, the ^{59}Fe(n, γ) production process competes with the ^{59}Fe β-decay to produce an appreciable amount of ^{60}Fe. This reaction pair dominates the nuclear reaction uncertainties in ^{60}Fe production, with ^{59}Fe(n, γ) being difficult to measure in nuclear laboratories due to its long lifetime and E1 and M1 reaction channels (Jones et al. 2019b). Using effective He-burning reaction rates can account for the correlated behavior of nuclear reactions and mitigate the overall nuclear uncertainties in these shell-burning environments (Austin et al. 2017). Astronomical observations of the ^{60}Fe/^{26}Al ratio will help to constrain the nuclear reaction aspects of massive stars, given the experimental difficulties in measuring all reaction channels involved at the astrophysically relevant energies.

Such comparison and interpretation, however, relies on the assumption that ^{26}Al and ^{60}Fe originate from the same sources (see, e.g., Timmes et al. 1995; Limongi & Chieffi 2006, 2013) and have similar diffuse emission distributions originating from nucleosynthesis in massive stars throughout the Galaxy. Therefore, the observational verification of the diffuse nature of ^{60}Fe emission is key to the above interpretation of measurements of an ^{60}Fe/^{26}Al ratio in terms of massive star models.

Several detections of ^{60}Fe-enriched material in various terrestrial as well as lunar samples (Knie et al. 2004; Wallner et al. 2015; Fimiani et al. 2016; Neuhäuser et al. 2019) confirm the evidence for a very nearby source for ^{60}Fe within several Myr. A signal from interstellar ^{60}Fe was first reported from the Na I spectrometer on board the *RHESSI* spacecraft (2.6σ), which was aimed at solar science (Smith 2004). They also presented a first upper limit of $\sim$0.4 (1σ) for the flux ratio of ^{60}Fe/^{26}Al γ-ray emissions (Smith 2004). The first solid detection of Galactic ^{60}Fe emission was obtained from *International Gamma-Ray Astrophysics Laboratory* (*INTEGRAL*) SPectrometer on *INTEGRAL* (SPI) measurements detecting ^{60}Fe γ-rays with a significance of 4.9σ after combining the signal from both lines at 1173 and 1332 keV (Wang et al. 2007), constraining the flux ratio of ^{60}Fe/^{26}Al γ-ray emissions to the range of 0.09–0.21 (Wang et al. 2007). Subsequent analysis of 10 yr *INTEGRAL*/SPI data with a different analysis method similarly suggested a ratio in the range $\sim$0.08–0.22 (Bouchet et al. 2015).

In this paper, we use more than 15 yr of SPI observations throughout the entire Galaxy and carry out a broadband spectral analysis in the γ-ray range 800–2000 keV. Rather than striving for high spectral resolution and line shape details, this wideband γ-ray study aims at studying both ^{60}Fe and ^{26}Al emission signals at 1173, 1332, and 1809 keV simultaneously, i.e., using identical data and analysis methods, including data selection and background treatments. This paper is structured as follows. In Section 2, we will describe the SPI observations and data analysis steps. Our emission models to describe the 800–2000 keV band are introduced in Section 3. We present our morphological and spectral findings in Section 4. Implications and conclusions are shown in Section 5.

2. Observations and Data Analysis

2.1. SPI Observational Data

The *INTEGRAL* mission (Winkler et al. 2003) began with its rocket launch on 2002 October 17. The SPI (Vedrenne et al. 2003) is one of *INTEGRAL*'s two main telescopes. It consists of 19 Ge detectors, which are encompassed in a BGO detector system used in anticoincidence for background suppression. The SPI has a tungsten coded mask in its aperture, which allows imaging with $\sim$3° resolution within a 16° × 16° fully coded field of view. The Ge detectors record γ-ray events from energies between 20 keV and 8 MeV. The performance of the detectors and the behavior and variations of the instrumental backgrounds have been studied over the mission and confirmed that scientific performance is maintained throughout the mission years (Diehl et al. 2018). The *INTEGRAL* satellite with its coaligned instruments is pointed at predesignated target regions, with a fixed orientation for intervals of typically $\sim$2000 s (referred to as *pointings*).

The basic measurement of SPI consists of event messages per photon triggering the Ge detector camera. We distinguish events that trigger a single Ge detector element only (hereafter *single event* (SE)) and events that trigger two Ge detector elements nearly simultaneously (hereafter *multiple event* (ME)). The fast pulse shape discriminator (PSD) electronic unit digitizes the shape of the current pulse and allows suppression of background events, e.g., from localized β-decays within the Ge detectors (Roques et al. 2003) or electronic noise. In this work, we use event data that hit only one detector (i.e., SE event data) and carry the PSD flag for acceptable pulse shape (event type PE).

We apply a selection filter to reject corrupted, invalid, or background-contaminated data. We apply selection windows to "science housekeeping" parameters such as the count rates in several background-monitoring detector rates, proper instrument status codes, and orbit phase. In particular, we use the SPI plastic scintillator anticoincidence counter mounted beneath the coded mask and the rate of saturating events in SPI's Ge detectors (i.e., events depositing >8 MeV in a single Ge detector, hereafter referred to as GeDSat rates) as background tracers. This selection leads to exclusions of strong solar-flare periods and other times of clearly increased/abnormal backgrounds. Additionally, the regular background increases during and after passages through the Earth's radiation belts are eliminated by a 0.1–0.9 window on orbital phase. As a final step after these primary selections, we perform a quality-of-fit selection using our best background model only (see Section 2.2) and exclude all further pointings that show deviations beyond 10σ above a fit of this background plus the expected signal contribution per pointing, thus eliminating pointings with abnormal background (note that SPI data are dominated by instrumental background counts, so source counts from diffuse emission such as ^{60}Fe alone cannot significantly deteriorate the fit to a pointing data set). These outliers are mainly due to missing "science housekeeping" parameters that are interpolated later or burst-like events in the

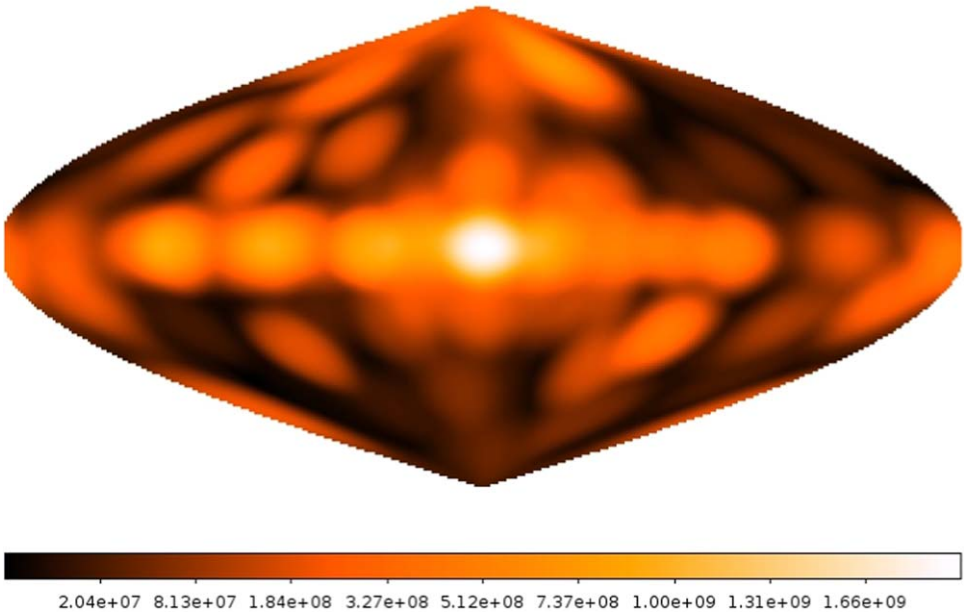

Figure 1. Exposure sky map of the fully coded field of view in Galactic coordinates (the number at the color bar in units of seconds) for the data selected from 15 yr SPI observations for our ^{60}Fe and ^{26}Al study (*INTEGRAL* orbits 43–1950).

field of view, for example, gamma-ray bursts, flares from X-ray binaries, or solar activity.

The resulting data set for our ^{60}Fe and ^{26}Al study encompasses 99,864 instrument pointings across the entire sky, equivalent to a total (deadtime-corrected) exposure time of 213 Ms. This includes data from *INTEGRAL* orbits 43–1950, or 2003 February to 2018 May. The sensitivity (effective exposure time, effective area) of the SPI observations is further reduced by the successive failure of four of the 19 detectors (2003 December, 2004 July, 2009 February 19, and 2010 May 27). In Figure 1, we show the resulting exposure map from our cleaned data set.

We bin detector events from the range between 800 and 2000 keV into seven energy bins: three of these address γ-ray line bands for ^{60}Fe and ^{26}Al (1169–1176, 1329–1336, and 1805–1813 keV), and four continuum bands in between (800–1169, 1176–1329, 1336–1805, and 1813–2000 keV) are added to robustly determine the line flux above the diffuse γ-ray continuum. In the Appendix, we present an investigation of the impact of event selections using the PSD (see Figure 12). The PSD selections succeed in suppressing apparent electronics noise that is visible in raw detector spectra in the energy range 1300–1700 keV. We therefore use such PSD selections, although the impact on the resulting spectra from celestial sources is not clear except for this continuum band (see Appendix).

2.2. Data Analysis

The raw data of SPI are dominated by the intense background radiation characteristic of platforms undergoing cosmic-ray (CR) bombardment. In SPI data analysis, we combine background models with a spatial model for sky emission to fit our data, allowing for adjustments of fit parameters for background and sky intensities. In general, the counts per energy bin, per detector, and per pointing are fitted by the background model described in Siegert et al. (2019), with details outlined shortly below, and the assumed sky map of celestial emission (e.g., the ^{26}Al distribution obtained by COMPTEL or exponential disk models; see Section 3) as convolved into the domain of the SPI data space for the complete pointing sequence by the instrument coded mask response,

$$D_{e,d,p} = \sum_{m,n}\sum_{j=1}^{k_1} A_{e,d,p}^{j,m,n}\,\beta_s^j I_j^{m,n} + \sum_{t}\sum_{i=1}^{k_2} \beta_{b,t}^i B_{e,d,p}^i + \delta_{e,d,p}, \quad (2)$$

where e, d, and p are indices for the data space dimensions (energy, detector, and pointing); m and n are indices for the sky dimensions (galactic longitude and latitude); A is the instrument response matrix; I is the intensity per pixel on the sky; k_1 is the number of independent sky intensity distribution maps; k_2 is the number of background components; and δ is the count residue after the fitting. The coefficients β_s for the sky map intensity are constant in time, while $\beta_{b,t}$ is allowed to be time dependent; see Section 2.3 below. The sky brightness amplitudes β_s comprise the resultant spectra of the signal from the sky. For this model-fitting analysis, we use a maximum-likelihood method, implementing Poisson statistics that apply to such a detector count analysis. Our software implementation is called *spimodfit* (Strong et al. 2005). The fitted model components are analyzed for further consistency checks on possible systematics in the residuals.

We thus derive, per energy bin, the best-fit parameter values with uncertainties and their covariance matrices. This provides flux estimates that are independent of spectral-shape expectations.

2.3. ^{60}Fe Background Characteristics

Much of the radiation from the instrumental background is promptly emitted directly from CR impacts. Background components arise from radioactive isotopes produced by the CR impacts. Local radioactivity in the spacecraft and instruments themselves will thus generate both broad continuum background emission and narrow gamma-ray lines from long- and short-lived radio-isotopes. Varying with energy, background components may exhibit complex time variability due to their origins from more than one physical source (Weidenspointner et al. 2003).

Background modeling by using the entire mission spectroscopy history has been established recently (Siegert et al. 2019).

For the energy bands studied here, we follow this general approach and model the background by fitting two components, one for the continuum and one for instrumental lines. From the mission spectral database (Diehl et al. 2018), we construct these background models at fine spectral precision. Then, we allow for adjustment of its overall normalization in intensity, which accounts for the fact that the (small) celestial signal that had been part of the mission data used for this database now needs to be separated out. The instrument records several detector triggers that have sufficiently high count rates, such as that of onboard radiation monitors, the SPI anticoincidence shield count rate, and the rate of saturating Ge detector events (events depositing >8 MeV in a Ge detector, GeDSat). These count rates reflect the current CR flux that causes the prompt instrumental γ-ray background, while the long-term trends of radioactive buildup and decays are inherent to the spectral background database. In this analysis, we use the GeDSat rates as a short-term background tracer and first-order description of the background variations with timescales of pointing-to-pointing from 800 to 2000 keV. This tracing is sufficient in energy bins at or below the instrumental resolution; however, in broader energy bins, such as used in this work, the superposition of the effects from different background lines blended together in a broader bin requires rescalings after suitable time intervals.

The coefficients $\beta_{b,t}$ for background normalizations are therefore allowed time dependent, to cater for such effects and different background normalizations for each camera configuration of 19/18/17/16/15 functional detector elements, as well as for possible variations on timescales shorter than our background model was built.

In Figure 3, we show the optimal renormalization timescale for the ^{60}Fe energy bin including the 1173 keV line. We find an optimum fit when renormalizing the background at a timescale of one orbit, which corresponds to 1674 background parameters per component. As a consistency check, we performed an estimate of the ^{60}Fe signal significance of the 1169–1176 keV band (continuum plus line), as could be expected from earlier measurements (Wang et al. 2007). In this estimation, we consider only the inner Galaxy and assume the COMPTEL ^{26}Al map as a tracer for the morphology of ^{60}Fe emission, and we adopt a total galaxy-wide flux of 4×10^{-4} ph cm^{-2} s^{-1}. We then make use of the approach by Vianello (2018), who extended the Bayesian significance estimates of Li & Ma (1983), and assume herein that our background model parameters are normally distributed. This obtains the black line shown in Figure 3, estimating a significance of 6σ for our optimal background model rescaling. In case about half of the flux of 4×10^{-4} ph cm^{-2} s^{-1} is degenerate and absorbed in the diffuse γ-ray continuum component, the line significance will be around 4σ in our estimate for a single line.

The background rescaling investigations in the remaining energy bins show similar optimum timescales, except for the lowest energy bin (800–1169 keV), which requires four parameters per orbit. The number of degrees of freedom is thus 1,591,831 for 1,595,180 data points in the ^{60}Fe, ^{26}Al, and higher-energy continuum bins, taking into account all fitted parameters for the sky, detector failures, and background variations.

Analyzing the resulting background variations in the ^{60}Fe line bands, we now investigate the candidate origins based on our detailed spectral analysis of the instrumental background with high spectral resolution. The most important background lines are

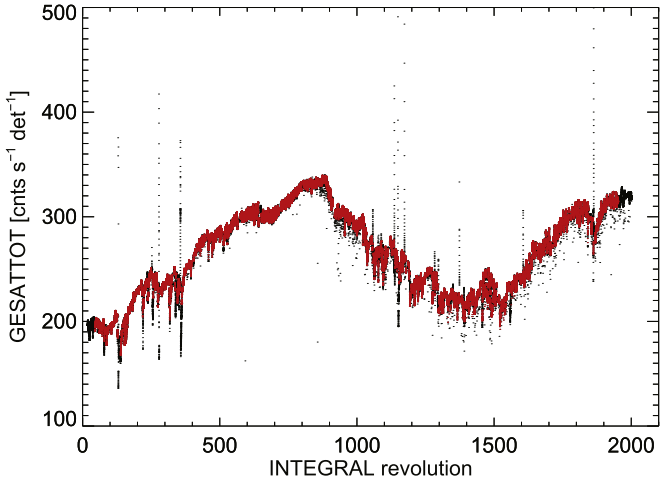

Figure 2. The SPI background tracer variations with time from saturated events in the Ge camera (GeDSat). In the panel, the full SPI database is shown in black, and the chosen data based on our selection criteria are in red.

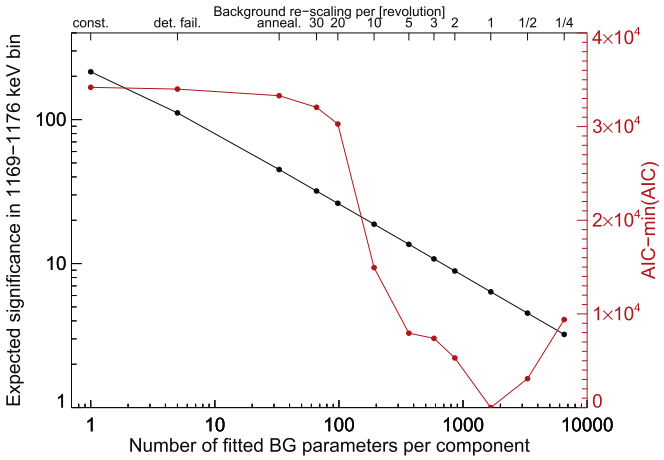

Figure 3. Expected significance (in σ units; black points) above a background-only description of the data in the 1169–1176 keV band, estimated from likelihood tests, background vs. background plus source, using different numbers of background parameters (bottom axis), i.e., varying the background on different timescales (top axis: number of *INTEGRAL* revolutions; or whenever an annealing was performed, a detector failed; or assuming a constant background). The red points show the AIC (AIC $= 2n_{\rm par} - 2\ln(L)$, where $n_{\rm par}$ is the total number of fitted parameters; right axis), which was used to find the required number of background parameters to describe the data in this bin sufficiently well. The optimum is found at one *INTEGRAL* orbit or 1674 background fit parameters. The black points show the expected significance in the band with a total flux of 4×10^{-4} ph cm^{-2} s^{-1} as a function of fitted background parameters. See text for details.

the ones expected from the decay of ^{60}Co in the instrument and satellite at the same line energies because this is the same cascade de-excitation in both cases. This ^{60}Co background builds up in intensity with time due to its 5.3 yr radioactive lifetime and thus will increasingly contribute to the total measured ^{60}Co γ-ray line signal. In addition, there is a strong background line from activated Ge at 1337 keV, which blends into the high-energy ^{60}Fe line at 1332 keV. This Ge line, however, shows no radioactive buildup, as the decay time is of the order of nanoseconds; hence, the count rate in this line closely follows the general activation of backgrounds. All of these lines are superimposed onto an instrumental continuum background that is dominated by bremsstrahlung inside the satellite and also includes Compton-scattered photons and a composite of weaker lines that escape

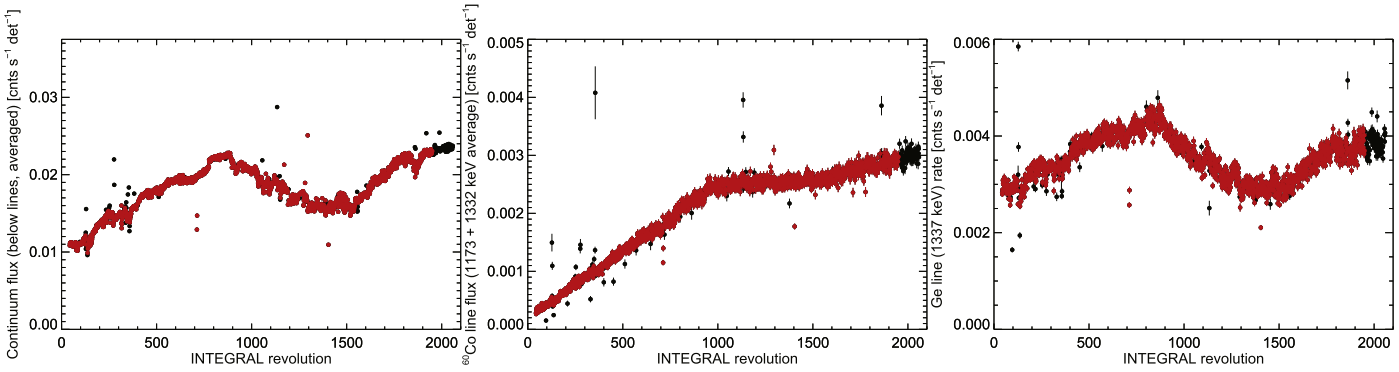

(a) Continuum intensity. (b) ^{60}Co line intensity. (c) Ge background line.

Figure 4. The SPI background continuum and line components relevant in the spectral regime of ^{60}Fe lines: (a) continuum count rate, (b) ^{60}Co activation, and (c) Ge activation line. In each panel, the full SPI database is shown in black, and the chosen data based on our selection criteria are in red.

identification in our deep spectral background analysis (Diehl et al. 2018). In Figures 2–3(c), we show the characteristic background components as they vary with time, as determined from our data set.

Here we focus on the total galactic emission, so that extrapolated estimates from the inner Galaxy toward the full Galaxy only may serve as guidance, rather than a precise prediction. Nevertheless, we see that the steadily rising ^{60}Co background line flux leads to a very shallow increase in the significance of celestial ^{60}Fe over time, shallower than the ^{60}Fe count accumulation alone would suggest. While our previous result with only 3 yr of data (Wang et al. 2007) showed a 4.9σ signal, in this case, using both ^{60}Fe lines together and both SE and ME (single- and multiple-trigger event types), which is consistent with our expectations, the increase of data by more than 200% in our current data set would result in only 6σ significance for SE and the two lines combined. We now also understand the additional background time variation: because the background line rate increases almost linearly (Figure 4(b)), fitting the background requires more parameters than typical for the SPI background that follows the solar cycle directly.

3. Modeling ^{60}Fe in the Milky Way

The ^{60}Fe signal is too weak to derive the spatial distribution or perform an imaging analysis. Therefore, we attempt to constrain the size of the ^{60}Fe emission region through fitting a parameterized geometrical model: an exponential disk profile (see Equation 3), and we determine the scale radius and scale heights. Doing this for all energy bins between 800 and 2000 keV, we obtain information on how this approach deals with known spatial distributions of γ-ray emission, thus helping to judge systematics limitations with the ^{60}Fe interpretation. The exponential disk models in this analysis have been adopted in the following form:

$$\rho(x, y, z) = A \exp(-R/R_0) \exp(-|z|/z_0),$$
$$\text{with } R = \sqrt{x^2 + y^2}. \quad (3)$$

In Equation (3), $\rho(x, y, z)$ is the 3D emissivity that is integrated along the line of sight (l/b) to produce maps of sky brightness with a pixel size of $1^\circ \times 1^\circ$. These maps are then folded through the coded mask response to create the expected count ratios for all selected pointings. The normalization A, equivalent to β_s^j in Equation (2), is determined (fitted) for a grid of scale radii R_0 and scale heights z_0 that we test. Here we use a grid of 16 R_0 values from 500 to 8000 pc in steps of 500 pc times 32 z_0 values between 10 and 460 pc in steps of 30 pc and between 500 and 2000 pc in steps of 100 pc. These models are independently fitted to all seven energy bins to obtain a likelihood chart for all morphologies tested. From this, we can determine both the best-fitting flux and the best scale dimensions of the emission, plus their uncertainties. Doing this in all of our energy bands, we can directly compare the emission size characteristics of ^{26}Al versus ^{60}Fe, obtaining systematics information from the continuum bands in between (i.e., possible biases for scale dimensions, influenced by the continuum below the lines).

All previous searches for ^{60}Fe (Harris et al. 2005; Wang et al. 2007; Bouchet et al. 2015) generally assumed that the ^{60}Fe diffuse emission follows the sky distribution of the ^{26}Al line. In this study, we explore the morphology of ^{60}Fe by comparing with ^{26}Al emission, as well as continuum emission. We test different tracers of potential candidate sources for ^{60}Fe emission and compare those tracer maps to that of ^{26}Al emission as measured and deconvolved from γ-ray data. This provides an independent judgment of how similar ^{60}Fe and ^{26}Al are (Section 4.3) compared to tracers that may include some of the expected deviations from a strict correlation with ^{26}Al. Similar to previous studies (Wang et al. 2009; Siegert 2017), we fit all-sky survey maps from a broad range of different wavelengths to our SPI data. From this, we obtain a qualitative measure that maps are favored at our chosen energies. We test a comprehensive set of maps to trace different emission mechanisms that may be related to our SPI data in the different energy bands. The list of tested maps (Table 1) also includes source tracers that may be weakly or not at all related to the candidate ^{26}Al and ^{60}Fe sources. We use this list of tracers for all of our energy bands in order to reveal degeneracies and systematics, because differences between maps are hard to quantify through fit likelihoods in absolute terms. We also include a background-only fit for reference. In Table 1, we briefly comment on each map to illustrate its main features.

4. Results

From independently fitting spatial emission models to SPI data for each of our seven energy bands, we obtain intensity values for the celestial emission detected in each of these bands for the same adopted spatial distribution model. In Table 2, we present the χ^2 values for seven energy bands in the modeling

Table 1
The Inventory of Candidate Source Tracers for Which We Compare How They Can Represent Emission in the Seven Energy Bands of SPI Measurements between 800 and 2000 keV

Energy	Tracer Type and Comments
408 MHz	Synchrotron emission of CR e-; mosaic Jodrell Bank/Effelsberg/Parkes (Haslam et al. 1982; Remazeilles et al. 2015)
21 cm	H I neutral hydrogen, Effelsberg-Bonn H I Survey (EBHIS; Kerp et al. 2011; Winkel et al. 2016)
1.25–4.9 μm	DIRBE infrared emission from starlight of M, K, and G stars, four individual maps (Hauser et al. 1998)
12–240 μm	IRAS infrared emission from dust, six individual maps (Hauser et al. 1998)
380–672 nm	Optical emission, all-sky mosaic from >3000 CCD frames (Mellinger 2009)
656 nm	Hα emission, partly ionized interstellar gas, star-forming regions (Haffner et al. 2016)
1.809 keV	^{26}Al decay emission from massive star groups, COMPTEL (Plüschke et al. 2001), and SPI (Bouchet et al. 2015)
1–30 MeV	COMPTEL MeV γ-rays, CR–ISM interactions (Schönfelder et al. 1993; Strong et al. 1994)
>100 MeV	EGRET 0.1–30 GeV band, CR–ISM interactions (Hartman et al. 1999)
1–3 GeV	*Fermi*/LAT, CR–ISM interactions, high-energy sources (Atwood et al. 2009)
0.25–1.5 keV	*ROSAT* all-sky survey, hot ISM, X-ray binaries, three individual maps (Snowden et al. 1997; Voges et al. 1999)
14–150 keV	*Swift*/BAT hard X-ray sources, X-ray binaries, pointlike, seven individual maps (Krimm et al. 2013)
30–857 GHz	Planck radio bands, nine individual maps, synchrotron emission, individual sources (Planck Collaboration et al. 2016)
30–857 GHz: AME	Anomalous microwave emission (Planck Collaboration et al. 2016)
30–857 GHz: CMB	Cosmic microwave background (Planck Collaboration et al. 2016)
30–857 GHz: CO	$J(1 \rightarrow 0)$ emission at 150 GHz (Planck Collaboration et al. 2016)
30–857 GHz: dust	⋯ (Planck Collaboration et al. 2016)
30–857 GHz: free–free	Bremsstrahlung emission (Planck Collaboration et al. 2016)
30–857 GHz: synchrotron	⋯ (Planck Collaboration et al. 2016)
30–857 GHz: SZ effect	Sunyaev–Zel'dovich effect (Planck Collaboration et al. 2016)
30–857 GHz: X-lines	Strong non-CO lines in the center of the Galaxy (Planck Collaboration et al. 2016)

Table 2
The χ^2 Values for the Analyzed Set of Seven Energy Bins from 800 to 2000 keV, Together with the Number of Degrees of Freedom and Fitted Parameters Here χ^2_P refers to Pearson χ^2, χ^2_Γ is Modified χ^2, and χ^2_Λ is Cstat χ^2 (see Mighell 1999)

Energy Bin (keV)	800–1169	1169–1176	1176–1329	1329–1336	1336–1805	1805–1813	1813–2000
χ^2_P	1,666,345	1,578,309	1,586,945	1574,026,	1,601,048	1,579,418	1,583,406
χ^2_Γ	1,666,705	1,577,964	1,586,890	1,574,878	1,600,992	1,579,990	1,583,382
χ^2_Λ	1,666,313	1,582,827	1,587,166	1,579,806	1,601,146	1,589,270	1,583,901
dof	1,591,831	1,591,831	1,591,831	1,591,831	1,591,831	1,591,831	1,591,831
Parameters	3349	3349	3349	3349	3349	3349	3349

fittings. So, the present fits are reliable, and the background model is acceptable.

For further discussion and analysis, we fit each extracted set of sky intensity values with

$$F(E;\, C_0,\, \alpha,\, F_{60},\, F_{26}) = C_0 \times \left(\frac{E}{1000\ \mathrm{keV}}\right)^{\alpha} + F_{60} \times (T(1172.5\ \mathrm{keV},\, 7\ \mathrm{keV}) + T(1332.5\ \mathrm{keV},\, 7\ \mathrm{keV})) + F_{26} \times T(1809.0\ \mathrm{keV},\, 8\ \mathrm{keV}), \quad (4)$$

where C_0 is the continuum flux density normalization at 1000 keV, α is the power-law index, and F_{60} and F_{26} are the integrated fluxes as derived from top-hat functions, $T(E_0, \Delta E)$, centered at E_0 with bin width ΔE. We link the parameters of the two ^{60}Fe lines, as they are expected to reflect the same incident flux in intensity and width. The lines are expected to be somewhat broadened above the instrumental line widths by 0.1–0.2 keV due to large-scale galactic rotation of sources (Wang et al. 2009; Kretschmer et al. 2013), and the instrumental line width would be ~2.8 keV around the ^{60}Fe lines and ~3.2 keV around the ^{26}Al line (Diehl et al. 2018). Within the 7 keV bins for the ^{60}Fe lines and the 8 keV bins for the ^{26}Al lines, 2.9σ (99.7%) of the expected line fluxes would be contained.

4.1. Characterizing the Extents of ^{60}Fe and ^{26}Al Emission

In Figure 5, we show the seven-band spectral intensities as derived from an exponential disk with a scale radius of 7 kpc and scale height of 0.8 kpc as a typical example. We selected this because it reflects the best-fit dimensions in the ^{26}Al line band. In this example, the continuum is determined as $(2.4 \pm 0.2) \times (E/1000\ \mathrm{keV})^{(-1.3\pm0.2)} \times 10^{-5}$ ph cm^{-2} s^{-1} keV^{-1}. The ^{60}Fe and ^{26}Al line fluxes are $(2.6 \pm 0.6) \times 10^{-4}$ and $(14.4 \pm 0.7) \times 10^{-4}$ ph cm^{-2} s^{-1}, respectively, which results in an ^{60}Fe/^{26}Al ratio of 18.3% ± 4.4%.

Our $16 \times 32 = 512$ scale size grid covers the full range of the Galactic plane and therefore provides a measure of the emission extents for ^{60}Fe and ^{26}Al, as well as for the continuum emission expected from bremsstrahlung and inverse Compton interactions of CR electrons. Each of the 512 exponential disk templates is treated individually in the first place, fitting its parameters without any priors or constraints. As a result, the absolute fluxes of the continuum and lines vary with the emission dimensions. We find that with larger-scale dimensions, the fluxes of the continuum and lines increase. We find no strong variation of the line-to-continuum ratio for either ^{60}Fe or ^{26}Al. This supports our assessment that the shape constraints that we derive are consistent and without major bias.

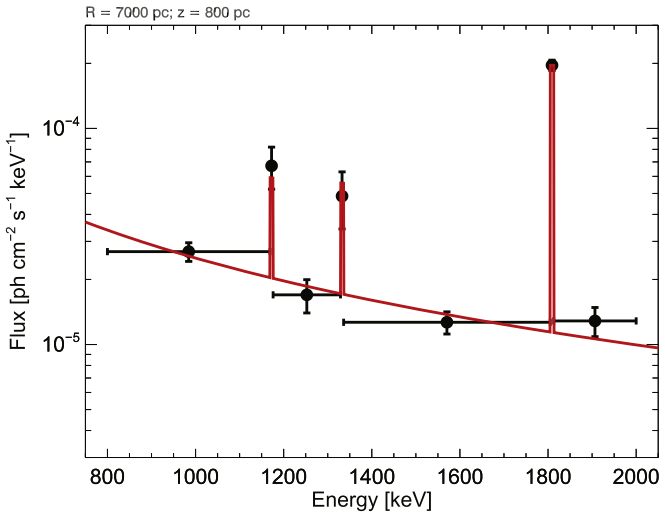

Figure 5. Spectral intensities (black) obtained from the fit to an exponential disk model with $R_0 = 7$ and $z_0 = 0.8$ kpc. The fitted total model, Equation (4), is shown in red.

The strong background line at 1337 keV (see Section 2) could affect the 1332 keV ^{60}Fe line result, which we therefore compare to the more isolated 1173 keV line; for our ^{60}Fe spatial results, we prefer to rely on the latter line for this reason, while the ^{60}Fe/^{26}Al flux ratio uses the data constraints from both Fe line bands combined. In our goal of determining the spatial extent of ^{60}Fe emission, for ^{60}Fe and ^{26}Al in the 1173 and 1809 keV lines, we show the likelihood contour regions versus scale heights and scale radii (in Figure 6) next to each other. For the ^{26}Al emission, we can obtain the characteristic scale radius of $R_0 = 7.0^{+1.5}_{-1.0}$ kpc and scale height of $z_0 = 0.8^{+0.3}_{-0.2}$ kpc. However, for the ^{60}Fe emission lines, the constraints are very poor due to the weak signals, formally resulting in $R_0 = 3.5^{+2.0}_{-1.5}$ and $z_0 = 0.3^{+2.0}_{-0.2}$ kpc. We will use the point-source model test to exclude one point-source model in the Galactic center (see Section 4.2).

In our goal to exploit maximum information for the ^{60}Fe/^{26}Al flux ratio while catering to the uncertainty of the spatial extent of ^{60}Fe emission, we include the quality of the fits to SPI data from this grid of exponential disk model fits in our assessment. We apply a weighting with the Akaike information criterion (AIC; Akaike 1974) derived from the likelihood and the number of fitted parameters in each energy bin, thus taking the individual measurement and fitting uncertainties of each model map into account. This yields an ^{60}Fe line flux value of $(3.1 \pm 0.6) \times 10^{-4}$ ph cm^{-2} s^{-1} and an ^{26}Al line flux of $(16.8 \pm 0.8) \times 10^{-4}$ ph cm^{-2} s^{-1}. The ^{60}Fe/^{26}Al ratio resulting from this emission extent–averaged analysis is 18.4% ± 4.2%. The derived ^{26}Al flux for the full Galaxy is also consistent with the previous ^{26}Al map study with SPI data (Bouchet et al. 2015). In addition, a recent SPI analysis reported the ^{26}Al flux values for both the inner Galaxy and the whole sky (Pleintinger et al. 2019): $\sim 0.29 \times 10^{-3}$ ph cm^{-2} s^{-1} for the inner region and $\sim(1.7\text{–}2.1) \times 10^{-3}$ ph cm^{-2} s^{-1} for the whole sky. We show the ^{60}Fe/^{26}Al ratio distribution from all 512 exponential disk configurations in Figure 7, also indicating characteristic uncertainties.

4.2. Point-source Model Test for the Galactic Plane

In this section, we aim to constrain the morphology of the weak ^{60}Fe in another way. We produced a catalog of point-source locations with $91 \times 21 = 1911$ entries between $l = -90°$–$90°$ and $b = -20°$–$20°$ in 2° steps. Then we used this catalog to test a point-source origin for both ^{26}Al and ^{60}Fe emission lines in the Galactic plane. In this way, in Figure 8, we can check if and how extended the ^{26}Al and ^{60}Fe emissions are. These morphology studies of ^{26}Al and ^{60}Fe emission distributions suggested that the γ-ray emissions are not attributed to one or several point sources in this region. In positive longitudes, the ^{26}Al emission extended to $l \sim 35°$, which may be contributed by Aquila, and at $l \sim 80°$, the emission structure is Cygnus. The truncated structure in positive longitudes will partially be the influence of the exposure map (see Figure 1). In the negative longitudes, the ^{26}Al emission extended to $l \sim -75°$, probably Carina. However, these maps should not be interpreted as the real sky distribution map but can imply that the emission is not pointlike. The use of this simplified emission model at different galactic coordinates would yield large residuals in the raw SPI data space. Likewise, the ^{60}Fe emission morphology is unknown and could be particularly similar to ^{26}Al.

From these trials, we can estimate the influence of diffuse or pointlike emission by taking into account that a background-only fit would result in test statistics (TS) defined as

$$\mathrm{TS} = 2(\log(L_{\mathrm{BG}}) - \log(L_{\mathrm{PS}}(l/b)), \quad (5)$$

with L_{BG} and L_{PS} being the likelihoods of a background-only fit and a background–plus–point source fit, respectively. For finding a point source by chance at a trial position (l/b), TS would be distributed as $0.5\chi^2$ with 3 degrees of freedom (2 position, 1 amplitude), we can compare how much the measured TS distributions deviate. A single point source would have one (or more) high points at high TS at a particular sharply defined TS value. We can see that the ^{60}Fe case is deviating from the background-only case in more than a few points and consistently for TS > 12 (Figure 9). This would be a signature of a diffuse signal for the ^{60}Fe emission. For comparison, the ^{26}Al line case is shown as well. Therefore, we can exclude a single strong point source in the galactic center, as well as somewhere else in this region, as the origin of the detected ^{60}Fe emission.

4.3. Investigations of Different Emission Tracers

In our effort to investigate the spatial distribution of ^{60}Fe emission, we fit the SPI data with a large set of maps representing different source tracers (see Table 1). These include the 408 MHz map reflecting CR electrons through their radio emission, CR-illuminated interstellar gas shining in GeV γ-rays, the COMPTEL and SPI maps reflecting ^{26}Al radioactivity, different sets of infrared emission, and X-ray emission maps. The fit quality of these maps can be compared through their different likelihood ratios, where we normalize to a background-only reference (Figure 10). For the ^{26}Al line, as expected, we again find as the best-fitting tracer map the SPI ^{26}Al line map that had been derived from a different data set and analysis method (Bouchet et al. 2015), which supports the consistency of our methods. For the ^{60}Fe line, the best-fitting tracer map turns out to be the DIRBE 4.9 μm map representing emission from small dust grains and starlight from mostly M-, K-, and G-type stars.

From our set of candidate source tracers, Table 1, we use the likelihood ratio of the combined continuum bins, the two ^{60}Fe lines, and the ^{26}Al line, each normalized to a background-only fit, as a measure of the significance of a signal from the sky. We

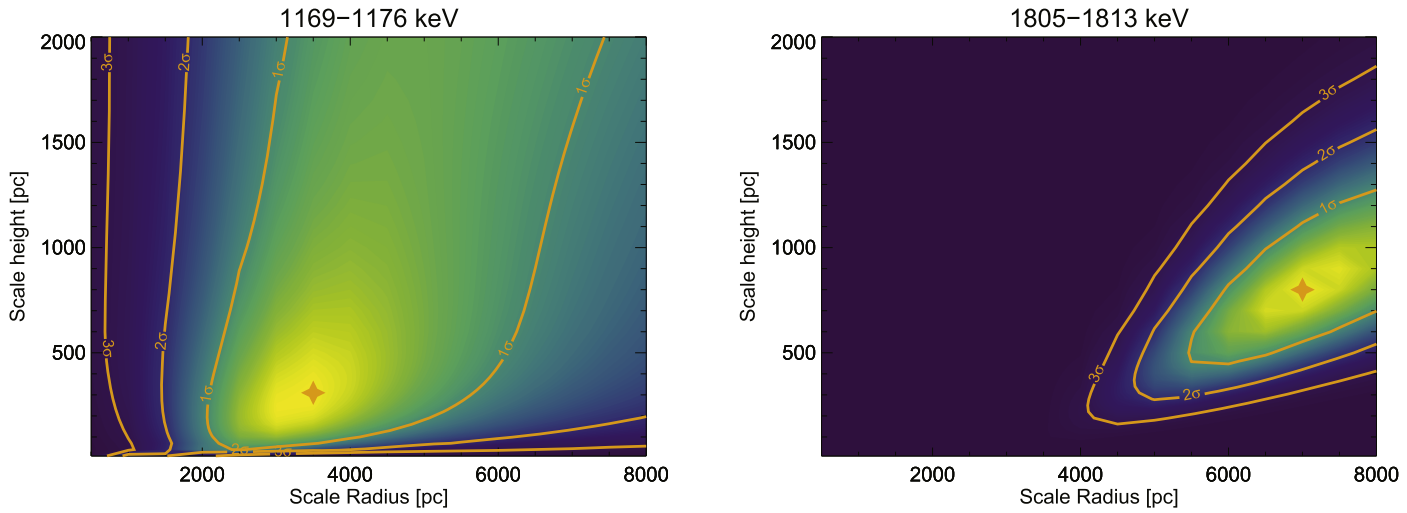

Figure 6. Two-dimensional likelihood profiles for exponential disk fits to SPI data as functions of scale radius and scale height. Shown are the 1σ, 2σ, and 3σ uncertainties, and the best-fit value is marked with a star symbol.

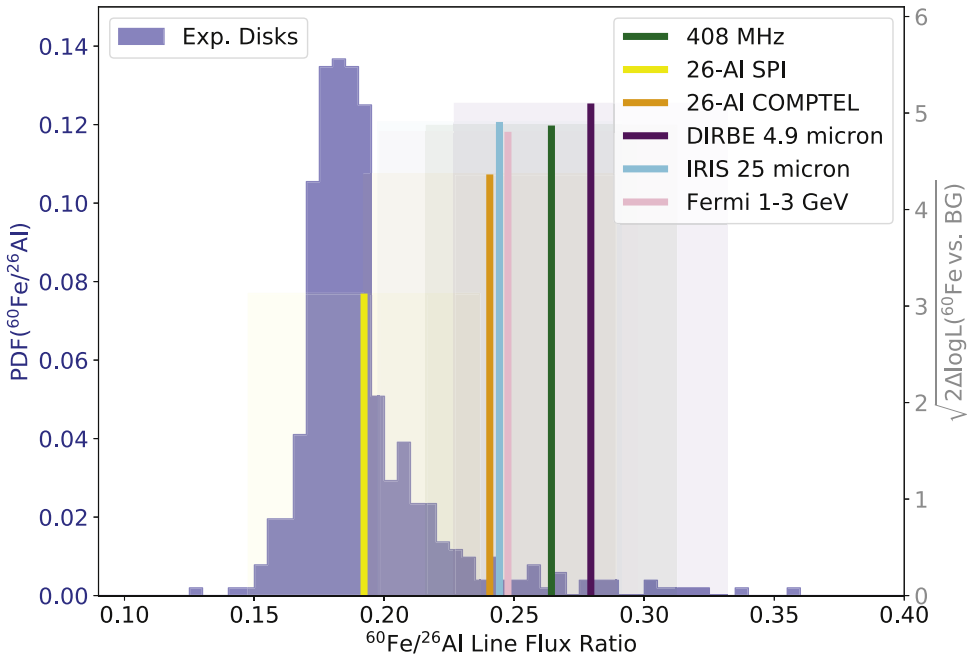

Figure 7. The ^{60}Fe/^{26}Al flux ratio for the grid of exponential disk models (blue; left axis). Including the uncertainties of the fluxes from each spectral fit, the total estimated ^{60}Fe/^{26}Al flux ratio from exponential disks is 18.4% ± 4.2%. Alternative to exponential disks, we also show the flux ratios derived from a set of tracer maps (see Section 4.2) as vertical lines according to their significance (right axis), together with their uncertainties as shaded bands. Clearly, these systematically show larger values compared to the exponential disk models. The IRIS (25 μm) map consistently shows the largest improvement above a background-only description for both lines (see Figure 11), so a flux ratio estimate from this map serves as a measure of the systematic uncertainty. We find a ratio of 0.24 ± 0.4 based on the IRAS 25 μm map, suggesting a systematic uncertainty of the order of 6%.

illustrate these signal significance levels and the resulting flux values in Figure 10.

For most of the tested maps, such as 408 MHz, IRAS 25 μm, COMPTEL ^{26}Al emission, GeV γ-ray emission, and CO/dust/free–free emission maps, both the ^{26}Al and ^{60}Fe radioactive-line bands show a significant detection of a signal from the sky in our SPI data set, with significance levels of $>16\sigma$ for the ^{26}Al line and $>4\sigma$ for the ^{60}Fe lines. In general, for the cases for which we obtain a significant ^{26}Al signal, such as the 408 MHz or COMPTEL ^{26}Al maps, ^{60}Fe also shows a significant signal above the background. Somewhat surprisingly, however, the SPI ^{26}Al map, which fits best at 1809 keV, is particularly poor in detecting sky emission in the 1173 keV line band of ^{60}Fe. This may be an indication that ^{26}Al and ^{60}Fe may indeed have a different emission morphology. In Figure 7, we also presented the ^{60}Fe/^{26}Al ratio ranges derived from these tracer maps with significant detections of both ^{26}Al and ^{60}Fe emission lines. The ^{26}Al all-sky emission maps observed by COMPTEL and SPI gave a ratio range of 0.15–0.24, and the 408 MHz, IRAS 25 μm, and *Fermi* γ-ray emission maps produced a ratio range of ∼0.2–0.3. The DIRBE 4.9 μm emission map can produce the highest detection significance level for ^{60}Fe lines, which gave an ^{60}Fe/^{26}Al ratio of 0.22–0.32.

For some cases, such as the hard X-ray map from *SWIFT*/BAT, the soft X-ray (0.25 keV) map from *ROSAT*, the Planck cosmic microwave background map, and the Sunyaev–Zel'dovich

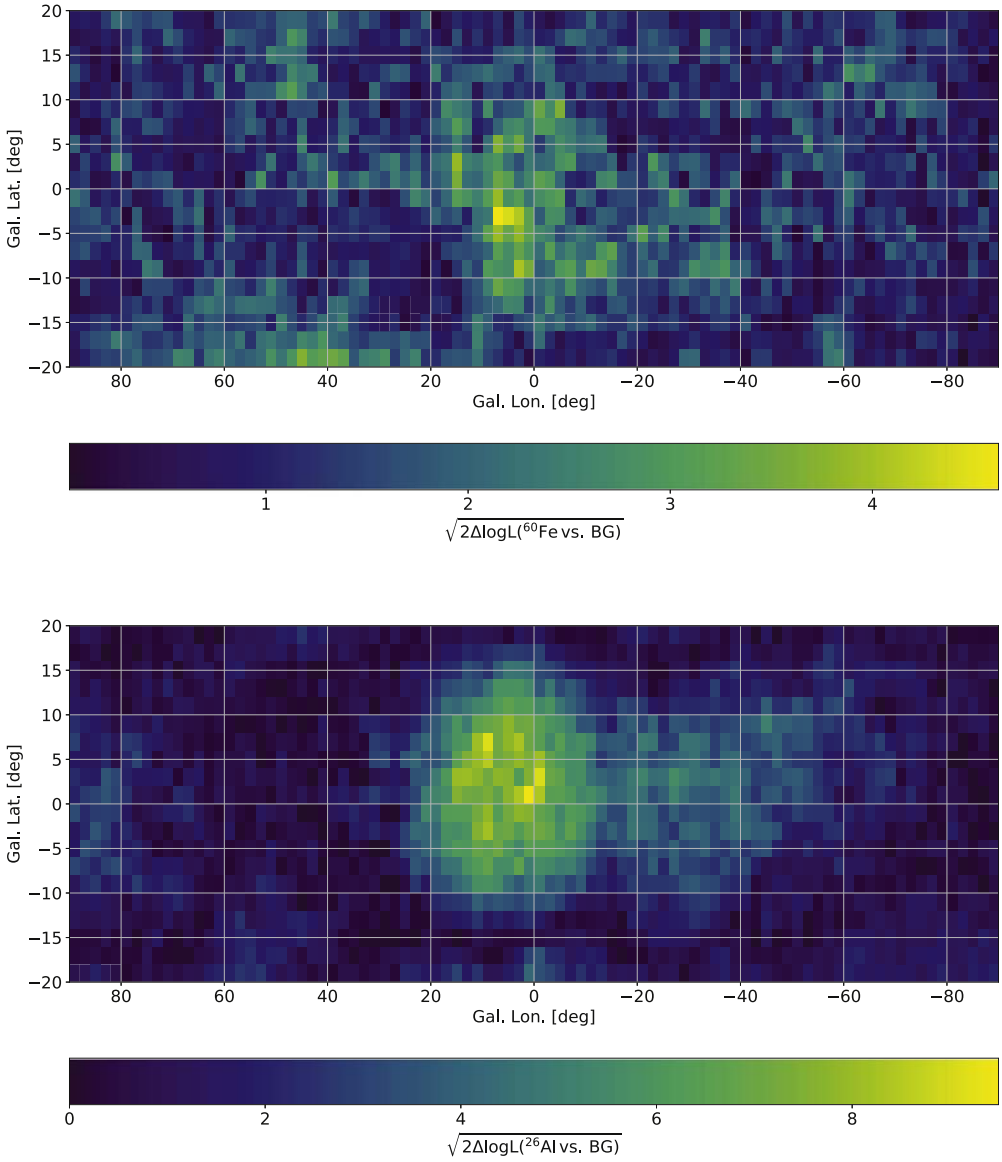

Figure 8. Summary of scanning the inner part of the Galactic plane for both ^{60}Fe (top) and ^{26}Al (bottom) line emissions ($-90° < l < 90°$, $-20° < b < 20°$) with individual point sources separated by 2° each. Each pixel in these visualizations represents one complete likelihood ratio test of background only vs. background plus point source; i.e., it includes all fitted parameters of the complete data set with one additional sky component, here modeled as a point source at Galactic coordinates (l/b). Each point is independent from all other points, as they represent another likelihood ratio test and thus may not be interpreted as linked to each other. The particular choice of fitting a single point source at individual positions stems from the fact that, within 3σ uncertainties, the exponential disk model extents (see Figure 7) are indistinguishable from a point source at the Galactic center. Thus, the opposite extreme of having only one or more point sources containing all of the flux is tested with this procedure.

effect map, in both the ^{26}Al and ^{60}Fe bands, we obtain no or at most marginal detections of sky emission. The hard X-ray map (100–150 keV) is dominated by emission of point sources along the Galactic plane, such as X-ray binaries. Therefore, the nondetection of signals in the ^{26}Al and ^{60}Fe bands would be in line with both the ^{26}Al and ^{60}Fe emission having a diffuse nature, rather than a strong contribution from such sources. The Planck Sunyaev–Zel'dovich effect map follows the distribution of clusters of galaxies, which are mainly located at high Galactic latitudes. The *ROSAT* soft X-ray (0.25 keV) map is also mostly bright at high Galactic latitude regions due to the strong soft X-ray absorption by the Galactic plane. Nondetection of ^{26}Al and ^{60}Fe emission signals with these two tracer maps is therefore consistent with our belief in the origins of ^{60}Fe and ^{26}Al signals in the plane of the Galaxy and its sources.

To compare the acceptable fits for the lines and continuum from the set of tracer maps, we show the sample spectra in our energy bands in Figure 11 from six typical all-sky distribution models, including the diffuse emission maps from observations (408 MHz, ^{26}Al γ-ray emission, infrared emission), analytical formulae (disk models), and point sources based on hard X-ray surveys. This provides an additional check against or insight into possible systematics in our spectral fit results.

4.4. The Diffuse γ-Ray Continuum

The hard X-ray to soft γ-ray Galactic diffuse emissions include continuum and γ-ray lines such as the positron annihilation line, ^{60}Fe emission lines, and ^{26}Al line. The diffuse continuum emission would originate from several physical processes: inverse Compton

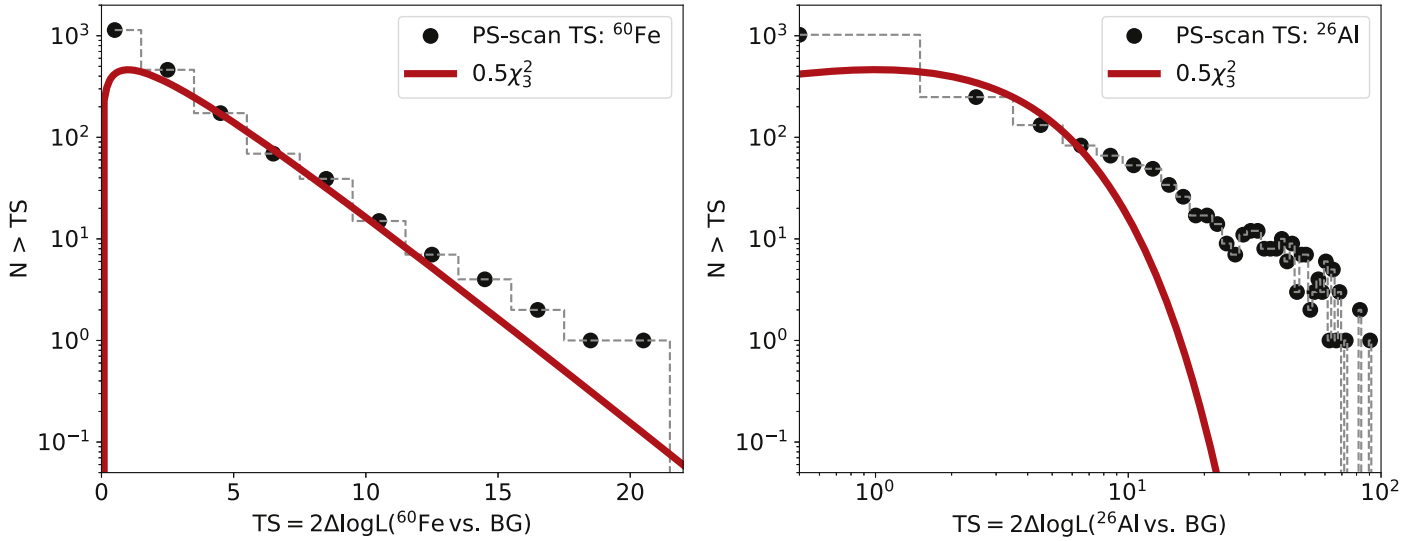

Figure 9. The TS in the ^{60}Fe and ^{26}Al lines, together with expectations from background-only fits, which would be distributed as $0.5\chi^2$ with 3 degrees of freedom. A single point source would have one (or maybe a few) value at high TS. Here ^{60}Fe is deviating from the background-only case in more than a few points and consistently for TS > 12.

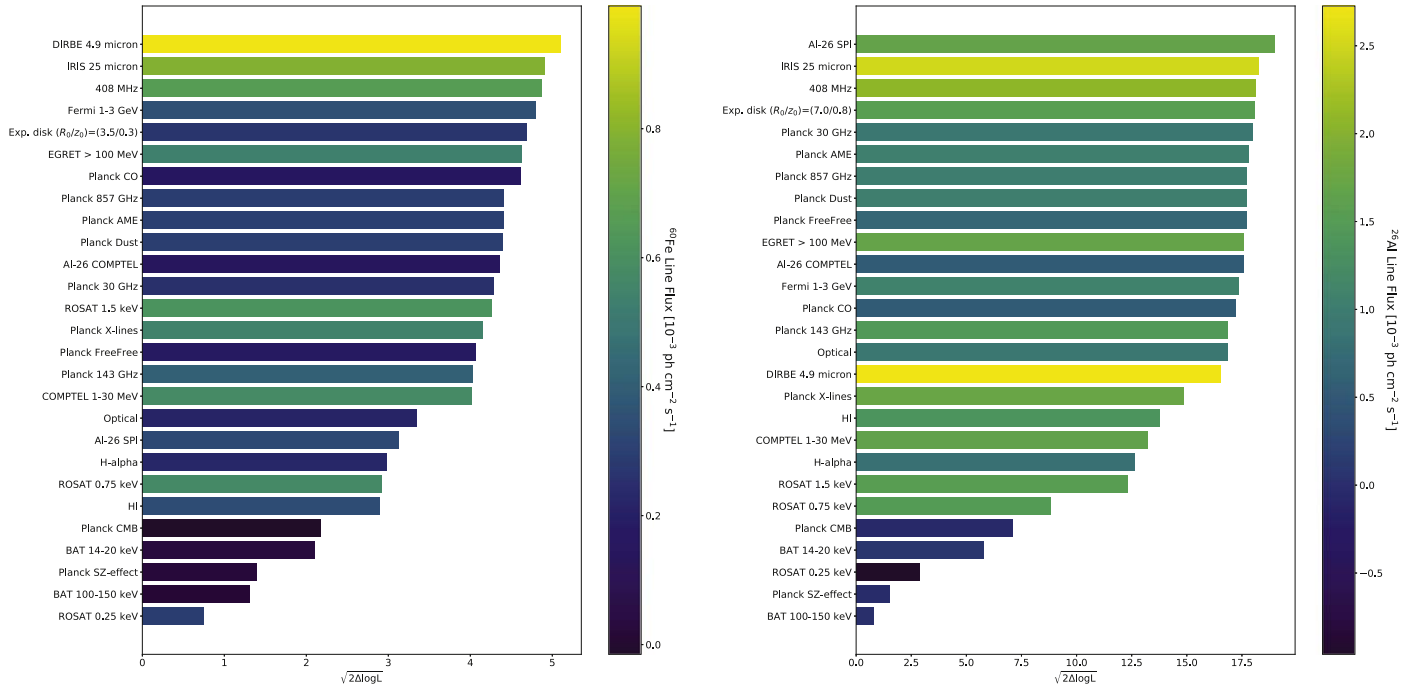

Figure 10. Likelihood ratio results for fits of different tracer maps (including the exponential disk maps) of candidate sources to the 1173 (left) and 1809 (right) keV data for ^{60}Fe and ^{26}Al emissions, respectively. The ratio was derived relative to the background-only fit. The fitted fluxes are given in color. For the ^{60}Fe lines, the best-fit sky distribution model is the DIRBE infrared emission map at 4.9 μm, while for the ^{26}Al line, the best fit is the ^{26}Al emission map derived by *INTEGRAL*/SPI.

scattering of the interstellar radiation field, bremsstrahlung on the interstellar gas from CR electrons and positrons, neutral pion decays produced in interactions of the CRs with the interstellar gas (see Strong et al. 2010 and references therein), and some unresolved hard X-ray/soft γ-ray sources.

With the 7 yr *INTEGRAL*/SPI observations, Bouchet et al. (2011) derived the hard X-ray spectrum from 20 keV to 2.4 MeV in the Galactic ridge region with a power-law index of $\Gamma \sim 1.4$–1.5 for the diffuse continuum and a flux level of $\sim 10^{-5}$ ph cm^{-2} s^{-1} keV^{-1}. Using the 15 yr SPI data covering 800 keV–2 MeV, we also determine the continuum spectra of the whole Galactic plane from the fittings, which have an average flux level of $\sim(2.0 \pm 0.4) \times 10^{-5}$ ph cm^{-2} s^{-1} keV^{-1} with a power-law index of $\Gamma \sim (1.3 \pm 0.2)$. The continuum flux derived in this work is fitted from the whole Galactic plane, rather than only from the inner Galactic ridge (Bouchet et al. 2011). The spectral indices are consistent with each other. We conclude that our broadband analysis also determines the Galactic continuum emission that underlies the targeted line emissions.

5. Summary and Discussion

With more than 15 yr of *INTEGRAL*/SPI observations, we carried out a wide range of spatial model fits to SPI data from 800

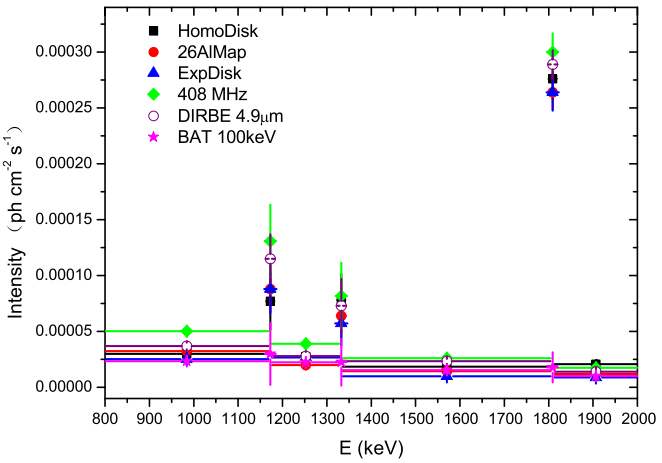

Figure 11. Comparison of the spectra from 800 to 2000 keV for different candidate source tracers in our continuum and line bands. We have included three γ-ray lines using six typical distribution models: a homogeneous disk model (constant brightness along the Galactic plane with scale height 200 pc; see Wang et al. 2009), a COMPTEL maximum entropy ^{26}Al emission map (Plüschke et al. 2001), an exponential disk model (scale radius 3.5 kpc, scale height 300 pc), the 408 MHz map (Remazeilles et al. 2015), the DIRBE infrared emission map at 2.5 μm (Hauser et al. 1998), and a hard X-ray sky map derived by *SWIFT*/BAT surveys from 100 to 150 keV (bright point sources; Krimm et al. 2013).

to 2000 keV in seven energy bands, including the line bands for ^{60}Fe at 1773 and 1332 keV and ^{26}Al at 1809 keV, as well as wider continuum energy bands around these. We clearly detected the signals from both ^{60}Fe and ^{26}Al emissions, as well as diffuse Galactic continuum emission. With only the SE database, assuming the exponential disk distribution model, we obtained a detection significance level of ^{60}Fe lines of $\sim 5.2\sigma$ with a combined line flux of $(3.1 \pm 0.6) \times 10^{-4}$ ph cm^{-2} s^{-1} and an ^{26}Al flux of $(16.8 \pm 0.7) \times 10^{-4}$ ph cm^{-2} s^{-1} for the whole Galaxy above the background continuum. From the consistent analysis approach with identical data selections, response, and background treatments, we minimize biases or systematics and obtain a result for the ^{60}Fe/^{26}Al flux ratio of 18.4% $\pm$ 4.2% based on the exponential disk grid maps. This large-scale galactic value is consistent with a local measurement from deposits of material on Earth (Feige et al. 2018). Since we do not know the real sky distribution of ^{60}Fe in the Galaxy, the derived ^{60}Fe/^{26}Al flux ratio will depend on the sky distribution tracers. In Figure 10, we compare the detection significance levels and flux values for ^{26}Al and ^{60}Fe using different sky distribution tracers. The best fits for ^{26}Al are the the SPI ^{26}Al and IRAS 25 μm maps, while for ^{60}Fe, the best ones are the DIRBE 4.9 μm and IRAS 25 μm maps. Thus, we can use these best-fit maps to constrain the uncertainties of the ^{60}Fe/^{26}Al flux ratio. If we use the same tracer for both ^{26}Al and ^{60}Fe, i.e., the IRAS 25 μm map, the ^{60}Fe/^{26}Al flux ratio is 0.20–0.28; then, using the different tracers, i.e., the SPI map for ^{26}Al and the DIRBE map for ^{60}Fe, one finds a ratio range of 0.30–0.44.

Using an astrophysically unbiased geometrical description of a double-exponential disk, we explore a broad range of emission extents along both Galactic longitude and latitude for ^{26}Al and ^{60}Fe. For ^{26}Al emission, we find $R_0 = 7.0^{+1.5}_{-1.0}$ and $z_0 = 0.8^{+0.3}_{-0.2}$ kpc. The ^{60}Fe γ-ray signal is weak and near the sensitivity limit of current γ-ray telescopes, so imaging similar to what is obtained for ^{26}Al γ-rays cannot be obtained at present. Formally, the scale radius and height are determined to be $R_0 = 3.5^{+2.0}_{-1.5}$ and $z_0 = 0.3^{+2.0}_{-0.2}$ kpc. We carried out a point-source model scan in the Galactic plane ($|l| < 90°$; $|b| < 20°$) for both ^{26}Al and ^{60}Fe emission line cases. The morphology and TS results suggest that the ^{60}Fe emission is not consistent with a strong single point source in the Galactic center or somewhere else in the Galactic plane. From our comparison with different sky maps, we provide the evidence for the diffuse nature of ^{60}Fe concentrated toward the Galactic plane, which is similar to that of ^{26}Al. But it is possible that the ^{26}Al and ^{60}Fe are distributed differently in the Galaxy.

The ratio of ^{60}Fe/^{26}Al has been promoted as a useful test of stellar evolution and nucleosynthesis models, because the actual source numbers and their distances cancel out in such a ratio. A measurement can, therefore, help theoretical predictions and shed light on model uncertainties, which are a result of the complex massive star evolution at late phases and related nuclear reaction rate uncertainties. Timmes et al. (1995) published the first detailed theoretical prediction of this ratio of yields in ^{60}Fe and ^{26}Al, giving a γ-ray flux ratio $F(^{60}\mathrm{Fe})/F(^{26}\mathrm{Al}) = 0.16 \pm 0.12$. With different stellar wind models and nuclear cross sections for the nucleosynthesis parts of the models, different flux ratios $F(^{60}\mathrm{Fe})/F(^{26}\mathrm{Al}) = 0.8 \pm 0.4$ were presented (Prantzos 2004). Limongi & Chieffi (2006) combined their yields for the stellar evolution of stars of different mass using a standard stellar mass distribution function to produce an estimate of the overall galactic ^{60}Fe/^{26}Al γ-ray flux ratio around 0.185 ± 0.0625. Woosley & Heger (2007) suggested that a major source of the large discrepancy was the uncertain nuclear cross sections around the creation and destruction reactions for the unstable isotopes ^{26}Al and ^{60}Fe that cannot be adequately measured in the laboratory. A new model of massive stars with the solar composition and the same standard stellar mass distributes from 13 to 120 $M_\odot$ compared yields with and without effects of rotation (Limongi & Chieffi 2013). For the models including stellar rotation, they determined a flux ratio of $F(^{60}\mathrm{Fe})/F(^{26}\mathrm{Al}) = 0.8 \pm 0.3$. For the nonrotation models, they obtained a flux ratio of $F(^{60}\mathrm{Fe})/F(^{26}\mathrm{Al}) = 0.2$–$0.6$, and if one only considers the production of stars from 13 to 40 $M_\odot$, the predicted flux ratio reduces to $\sim 0.11 \pm 0.04$. For stars more massive than 40 $M_\odot$, the stellar wind and its mass-loss effects on stellar structure and evolution contribute major uncertainty in ^{60}Fe ejecta production. But these stars may not actually explode as supernovae, but rather collapse to black holes, so their contributions may not be effective and could be ignored in a stellar mass–weighted galactic average. The measured values from γ-rays suggest that the (generally) higher values from theoretical predictions may overestimate ^{60}Fe and/or underestimate ^{26}Al production. This could be related to the explodability of massive stars for very massive stars beyond 35 or 40 $M_\odot$.

We are grateful to the referee for the fruitful suggestions to improve the manuscript. W.W. is supported by the National Program on Key Research and Development Project (grant No. 2016YFA0400803) and the NSFC (11622326 and U1838103). T.S. is supported by the German Research Society (DFG-Forschungsstipendium SI 2502/1-1). The *INTEGRAL*/SPI project has been completed under the responsibility and leadership of CNES; we are grateful to ASI, CEA, CNES, DLR (Nos. 50OG 1101 and 1601), ESA, INTA, NASA, and OSTC for support of this ESA space science mission.

Appendix

In Figure 12, we present the spectral examples from 800 to 2000 keV for the seven energy bands for both SE and PSD data

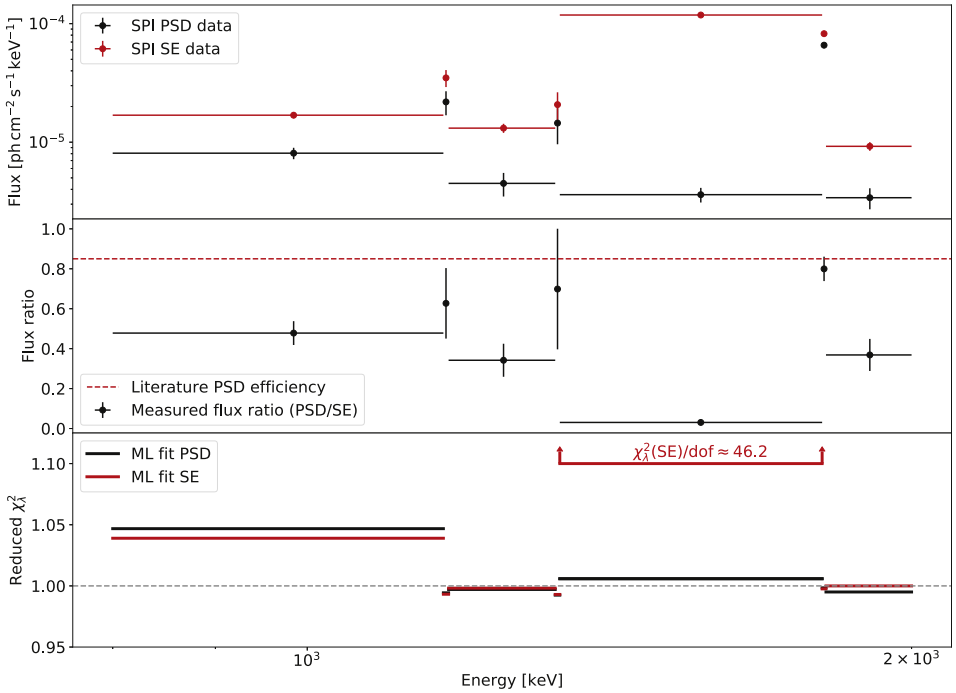

Figure 12. Comparison between the fitted broad spectra derived by the SE and PSD data sets from 800 to 2000 keV. In the band of 1336–1805 keV, the strong electronic noise cannot be suppressed in the case of SE.

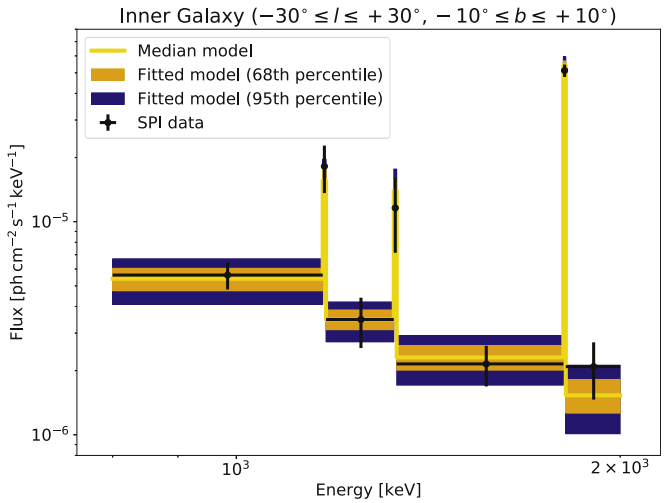

Figure 13. Fitted broad spectrum derived from the COMPTEL ^{26}Al map only for the inner Galaxy $-30° < l < 30°$, $-10° < b < 10°$. From this fitting, we derive the combined ^{60}Fe flux of $(4.5 \pm 0.8) \times 10^{-5}$ ph cm^{-2} s^{-1} and the ^{26}Al flux of $(2.60 \pm 0.13) \times 10^{-4}$ ph cm^{-2} s^{-1}. These values are consistent with the results in our previous work (Diehl et al. 2006; Wang et al. 2007, 2009).

sets. In the case of SE, the strong electronic noise cannot be suppressed in the band of 1336–1805 keV, while this electronic noise does not affect the spectral counts for the PSD data set. The reader can also refer to the supplementary information in Siegert et al. (2016), where we have done the test on the pulse shape selections. Thus, in this work, we only refer to the PSD data set.

In the present work, we have tried to constrain the sky distributions of ^{60}Fe and ^{26}Al lines in the Galaxy, so we determine the γ-ray spectra of three γ-ray lines (1173, 1332, and 1809 keV) for the entire sky. In the previous work (Wang et al. 2007, 2009), we studied the spectra and fluxes of ^{60}Fe and ^{26}Al using only the maps covering the inner Galaxy ($-30° < l < 30°$, $-10° < b < 10°$). In this appendix (see Figure 13), we also show the spectral fitting of the broad spectrum with the same map as in Wang et al. (2007, 2009) for comparison. For the inner Galaxy region, the ^{26}Al flux is determined to be $(2.60 \pm 0.13) \times 10^{-4}$ ph cm^{-2} s^{-1}, and the combined ^{60}Fe flux value is $(4.5 \pm 0.8) \times 10^{-5}$ ph cm^{-2} s^{-1}. These flux value levels are consistent with the previous work (Diehl et al. 2006; Wang et al. 2007, 2009; Bouchet et al. 2015). Based on the used COMPTEL ^{26}Al map in the inner Galaxy, the ^{60}Fe/^{26}Al flux ratio is 0.17 ± 0.03, consistent with the estimates from the full Galaxy, with smaller uncertainties because of the larger average exposure and increased signal-to-noise ratio when more flux is actually expected in the analyzed region. Of course, for the inner Galaxy, the diffuse γ-ray continuum has a mean flux of $(4.3 \pm 0.6) \times 10^{-6}$ ph cm^{-2} s^{-1} keV^{-1} at 1 MeV with a spectral index of 1.7 ± 0.3.

ORCID iDs

A. Heger https://orcid.org/0000-0002-3684-1325

References

Akaike, H. 1974, ITAC, 19, 716
Atwood, W. B., Abdo, A. A., Ackermann, M., et al. 2009, ApJ, 697, 1071
Austin, S. M., West, C., & Heger, A. 2017, ApJL, 839, L9
Bouchet, L., Jourdain, E., & Roques, J. P. 2015, ApJ, 801, 142
Bouchet, L., Strong, A. W., Porter, T. A., et al. 2011, ApJ, 739, 29
Diehl, R. 2013, RPPh, 76, 026301
Diehl, R., Dupraz, C., Bennett, K., et al. 1995, A&A, 298, 445
Diehl, R., Halloin, H., Kretschmer, K., et al. 2006, Natur, 439, 45
Diehl, R., Siegert, T., Greiner, J., et al. 2018, A&A, 611, 12
Feige, J., Wallner, A., Altmeyer, R., et al. 2018, PhRvL, 121, 221103
Fimiani, L., Cook, D. L., Faestermann, T., et al. 2016, PhRvL, 116, 151104
Haffner, L. M., Reynolds, R. J., Babler, B. L., et al. 2016, AAS Meeting, 227, 347.17
Harris, M. J., Knödlseder, J., Jean, P., et al. 2005, A&A, 433, L49
Hartman, R. C., Bertsch, D. L., Bloom, S. D., et al. 1999, ApJS, 123, 79
Haslam, C. G. T., Salter, C. J., Stoffel, H., & Wilson, W. E. 1982, A&AS, 47, 1
Hauser, M. G., Arendt, R. G., Kelsall, T., et al. 1998, ApJ, 508, 25
Jones, S., Röpke, F. K., Fryer, C., et al. 2019a, A&A, 622, 74
Jones, S., Röpke, F. K., Pakmor, R., et al. 2016, A&A, 593, 72

Jones, S. W., Möller, H., Fryer, C. L., et al. 2019b, MNRAS, 485, 4287
Kerp, J., Winkel, B., Bekhti, N., Flöer, L, & Kalberla, P. M. W. 2011, AN, 332, 637
Knie, K., Korschinek, G., Faestermann, T., et al. 2004, PhRvL, 93, 171103
Kretschmer, K., Diehl, R., Krause, M., et al. 2013, A&A, 559, 99
Krimm, H. A., Holland, S. T., Corbet, R. H. D., et al. 2013, ApJS, 209, 14
Li, T.-P., & Ma, Y.-Q. 1983, ApJ, 272, 317
Limongi, M., & Chieffi, A. 2003, ApJ, 592, 404
Limongi, M., & Chieffi, A. 2006, ApJ, 647, 483
Limongi, M., & Chieffi, A. 2013, ApJ, 764, 21
Lugaro, M., Doherty, C. L., Karakas, A. I., et al. 2012, M&PS, 47, 1998
Mahoney, W. A., Ling, J. C., Jacobson, A. S., & Lingerfelter, R. E. 1982, ApJ, 262, 742
Mellinger, A. 2009, PASP, 121, 1180
Mighell, K. J. 1999, ApJ, 518, 380
Neuhäuser, R., Giessler, F., & Hambaryan, V. V. 2019, MNRAS, in press
Ostdiek, K. M., Anderson, T. S., Bauder, W. K., et al. 2017, PhRvC, 95, 055809
Pignatari, M., Herwig, F., Hirschi, R., et al. 2016, ApJS, 225, 24
Planck Collaboration, Adam, R., Ade, P. A. R., et al. 2016, A&A, 594, A8
Pleintinger, M. M., Siegert, T., Diehl, R., et al. 2019, A&A, 632, 73
Plüschke, S., Dieh, R., Schönfelder, V., et al. 2001, in ESA SP 459, Exploring the gamma-ray universe, ed. B. Battrick et al. (Noordwijk: ESA), 55
Prantzos, N. 2004, A&A, 420, 1033
Prantzos, N., & Diehl, R. 1996, PhR, 267, 1
Rauscher, T., Herger, A., Hoffman, R. D., & Woosley, S. E. 2002, ApJ, 576, 323
Rauscher, T., Herger, A., Hoffman, R. D., & Woosley, S. E. 2003, NuPhA, 718, 463
Remazeilles, M., Dickinson, C., Banday, A. J., Bigot-Sazy, M.-A., & Ghosh, T. 2015, MNRAS, 451, 4311
Roques, J. P., Schanne, S., von Kienlin, A., et al. 2003, A&A, 411, L91
Rugel, G., Faestermann, T., Knie, K., et al. 2009, PhRvL, 103, 072502
Schönfelder, V., Bennett, B., Bloemen, H., et al. 1993, AdSpR, 13, 647
Siegert, T. 2017, PhD thesis, TU Munich
Siegert, T., Diehl, R., Greiner, J., et al. 2016, Natur, 531, 341
Siegert, T., Diehl, R., Weinberger, C., et al. 2019, A&A, 626, 73
Smith, D. M. 2004, ESA-SP, 552, 45
Snowden, S. L., Egger, R., Freyberg, M. J., et al. 1997, ApJ, 485, 125
Strong, A. W., Bennett, B., Bloemen, H., et al. 1994, A&A, 292, 82
Strong, A. W., Diehl, R., Halloin, H., et al. 2005, A&A, 444, 495
Strong, A. W., Porter, T. A., Digel, S. W., et al. 2010, ApJL, 722, L58
Sukhbold, T., Ertl, T., Woosley, S. E., Brown, J. M., & Janka, H.-T. 2016, ApJ, 821, 38
Timmes, F. X., Woolsey, S. E., Hartmann, D. H., et al. 1995, ApJ, 449, 204
Tur, C., Heger, A., & Austin, S. M. 2010, ApJ, 718, 357
Vedrenne, G., Roques, J.-P., Schönfelder, V., et al. 2003, A&A, 411, L63
Vianello, G. 2018, ApJS, 236, 17
Voges, W., Aschenbach, B., Boller, Th., et al. 1999, A&A, 349, 389
Voss, R., Diehl, R., Hartmann, D. H., et al. 2009, A&A, 504, 531
Wallner, A., Bichler, M., Buczak, K., et al. 2015, PhRvL, 114, 041101
Wanajo, S., Janka, H.-T., & Müller, B. 2013, ApJL, 774, L6
Wanajo, S., Müller, B., Janka, H.-T., & Heger, A. 2018, ApJ, 852, 40
Wang, W., Harris, M. J., Diehl, R., et al. 2007, A&A, 469, 1005
Wang, W., Lang, M. G., Diehl, R., et al. 2009, A&A, 496, 713
Weidenspointner, G., Kiener, J., Gros, M., et al. 2003, A&A, 411, L113
Winkel, B., Kerp, J., Kalberla, P. M. W., et al. 2016, A&A, 585, A41
Winkler, C., Courvoisier, T. J., Di Cocco, G., et al. 2003, A&A, 411, L1
Woosley, S. E. 1997, ApJ, 476, 801
Woosley, S. E., & Heger, A. 2007, PhR, 442, 269
Woosley, S. E., & Weaver, T. A. 1995, ApJS, 101, 181